THE JOURNAL OF PHYSICAL CHEMISTRY C

pubs.acs.org/JPCC Article

Understanding Solid–Gas Reaction Mechanisms by Operando Soft X-Ray Absorption Spectroscopy at Ambient Pressure

Luca Braglia,[○] Martina Fracchia,[○] Paolo Ghigna,* Alessandro Minguzzi,* Daniela Meroni, Raju Edla, Matthias Vandichel,* Elisabet Ahlberg, Giuseppina Cerrato, and Piero Torelli

Cite This: *J. Phys. Chem. C* 2020, 124, 14202–14212 Read Online

ACCESS | Metrics & More | Article Recommendations | Supporting Information

ABSTRACT: Ambient-pressure operando soft X-ray absorption spectroscopy (soft-XAS) was applied to study the reactivity of hydroxylated SnO_2 nanoparticles toward reducing gases. H_2 was first used as a test case, showing that the gas phase and surface states can be simultaneously probed: Soft-XAS at the O K-edge gains sensitivity toward the gas phase, while at the Sn $M_{4,5}$-edges, tin surface states are explicitly probed. Results obtained by flowing hydrocarbons (CH_4 and CH_3CHCH_2) unequivocally show that these gases react with surface hydroxyl groups to produce water without producing carbon oxides and release electrons that localize on Sn to eventually form SnO. The partially reduced SnO_{2-x} layer at the surface of SnO_2 is readily reoxidized to SnO_2 by treating the sample with O_2 at mild temperatures (>200 °C), revealing the nature of "electron sponge" of tin oxide. The experiments, combined with DFT calculations, allowed devising of a mechanism for dissociative hydrocarbon adsorption on SnO_2, involving direct reduction of Sn sites at the surface via cleavage of C–H bonds and the formation of methoxy- and/or methyl-tin species at the surface.

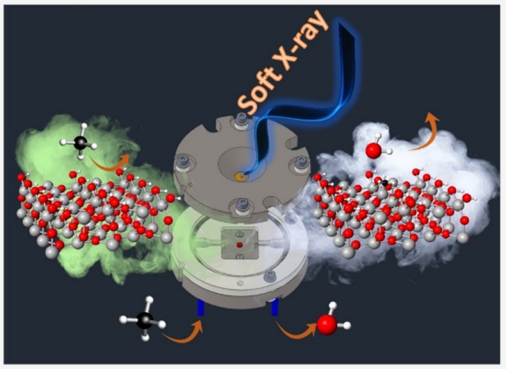

INTRODUCTION

Understanding the mechanism of solid/gas chemical reactions is crucial in many processes, either at low (e.g., fuel cells) and at mid-high temperatures (hydrocarbon chemistry, sensors, etc.). A major example is the mechanism of high-temperature gas sensing on semiconducting materials, where the interaction of the analyte with the solid surface is the key factor for the correct behavior of the sensor; however, the detailed mechanism of this interaction is still unclear. Similarly, hydrocarbon oxidation (C–H activation) on metal oxide catalysts is a rather unknown process, yet of paramount importance in several fields.

Semiconducting oxides such as SnO_2 act as gas sensors as their surface conductivity changes in response to variation of the surrounding atmosphere.[1−3] The adsorption of gas molecules supplies donor or acceptor levels in dependence on the reductive or oxidative nature of the analyte compared to molecular oxygen. While a number of comprehensive review articles and books dealing with the mechanisms of semiconducting oxides and the various aspects involved in gas-sensing processes have been published,[2,4−6] a general consensus toward a unified model describing their functioning is still lacking.[7−13] SnO_2 has also a wide range of applications as a catalyst for oxidation reactions, for example, the CO/O_2 and CO/NO reactions, suggesting that the ease of oxidation/reduction of surface states plays a major role in the reaction mechanisms.[14]

A complete understanding of the reaction mechanism, including the generation of byproducts in both phases and/or at the interface is required in order to design tailored materials. As it happens in the study of any heterogeneous phenomenon, conventional investigation methodologies give either unclear or incomplete information. The main reason is that typical probes focus on a single "actor" of the reaction (i.e., catalyst surface, adsorbed intermediates, and gas phase). In the best case, as for the so-called hyphenated techniques, two or more probes are used to monitor different portions of the interface. However, no single operando (i.e., under operative conditions) technique is capable to simultaneously look at highly complex processes from several perspectives, considering all parts of the interface (gas, solid surface, and adsorbed intermediates) and the relevant events occurring in mutual correlation.

A correlated problem is the real nature of the surface. Water species are ubiquitous on oxide surfaces, and these species are then expected to play a role in the surface reactivity. For example, it has been demonstrated that CO_2 cannot be adsorbed on heat-treated SnO_2 in dry air.[15] As the relative

Received: March 23, 2020
Revised: May 7, 2020
Published: June 5, 2020

https://dx.doi.org/10.1021/acs.jpcc.0c02546
J. Phys. Chem. C 2020, 124, 14202–14212

humidity increases, CO_2 is adsorbed, forming carbonate on the surface. When the surface is fully hydroxylated, carbonate is adsorbed by replacing surface −OH groups.[15] However, the presence of hydroxyl groups is scarcely taken into account when dealing with the mechanisms of adsorption on SnO_2: This is mainly due to the lack of established tools for looking at oxide surfaces in real operando conditions.

A wide collection of invaluable probes in material science is provided by synchrotron-based hard X-ray techniques: Hard X-ray diffraction and spectroscopies are presently the working horses of material characterization, both ex and in situ. For example, hard X-ray absorption spectroscopy (XAS) is an irreplaceable tool in the investigation of local atomic and electronic structures of materials.[16,17] Moreover, operando XAS experiments with hard X-rays are well-established, and almost every experimental condition can be reached to simulate realistic reaction environments.[18−20] On the contrary, in the soft X-ray regime, the applications of XAS (soft-XAS) in material science were substantially limited to a "surface science" approach, i.e., to the study of clean surfaces in high-vacuum conditions. In fact, the low penetration depth of X-rays with energies lower than 1 keV and the severe vacuum limitation have somehow hindered the development of operando experiments. However, soft-XAS is expected to give invaluable information for a complete understanding of the mechanisms of phenomena taking place at material surfaces and interfaces, such as catalysis, intercalation, electrochemistry, etc. Until now, these subjects have been mainly the playground of X-ray photoelectron spectroscopy (XPS), which is indeed sensitive to the immediate surface. However, despite some latest developments,[21] even in the near-ambient-pressure variant (NAP-XPS), the experiments are conducted in the mbar or tens of mbar range, which is very far from real working conditions. In this sense, soft-XAS was recently pushed forward in order to overcome this so-called "pressure gap".[22] For instance, transmission mode and fluorescence mode cells for soft-XAS have been developed, allowing operando investigations, for example, in the field of electrochemistry;[23−25] only very recently, specific reaction cells were designed for the study of catalyst or electrode surfaces at high temperature and at atmospheric pressure.[26−32] In these cases, soft-XAS is operated in the total electron yield (TEY) detection method, which renders the technique intrinsically surface-sensitive, and allows effective probing of the pertinent surface states. Indeed, in the TEY mode, all electrons (photoelectrons, Auger electrons, and secondary electrons) emitted from the sample after photoabsorption are collected. Since the escape depth of such electrons at moderate kinetic energies is very small (of the order of few nanometers), only very few atomic layers below the surface can be probed.

In this work, we further push forward soft-XAS operando experiments by demonstrating that the surface states and the reaction products at a solid/gas interface in solid/gas heterogeneous process can be probed simultaneously at ambient pressure and in a wide range of temperatures. It is clear from all of the above that soft-XAS in situ and/or operando conditions will allow us to obtain fundamental information in this case. If reactions taking place on oxide surfaces are considered, oxygen states are expected to be deeply involved; in addition, gas-phase water can be formed through reaction(s) involving surface hydroxyl groups. All these oxygen species can be easily detected at the O K-edge at 543.1 eV, i.e., well within the soft X-ray regime. Furthermore, the $M_{4,5}$-edges of tin at ca. 485−495 eV are close in energy and can be probed in the same experiment, thus permitting access of all valence states of the materials, searching for variations in the oxidation state of Sn.[33,34]

We performed experiments at the O K- and Sn $M_{4,5}$-edges at ambient pressure with the aim of studying the mechanisms of the surface reaction with reducing (H_2, CH_4, and CH_2CHCH_3) gases by SnO_2 nanoparticles. The investigation was conducted in the 100−360 °C temperature range, which nicely fits the operative range of the nanoparticles as a gas sensor.[35] In these conditions, the SnO_2 nanoparticles are free of physisorbed water, but chemisorbed, hydroxylated species are still present. H_2 was chosen as a test gas to assess the capability of XAS to simultaneously detect water in the gas phase at the O K-edge and reduced Sn species in the nanoparticles at the Sn $M_{4,5}$-edges. For what concerns CH_4 and CH_2CHCH_3, the results unequivocally show that hydrocarbons react with surface-hydroxylated species and release electrons that localize on Sn states to eventually form a SnO layer. This mechanism for the reactive adsorption of hydrocarbons on SnO_2 was finally tested against DFT calculations.

EXPERIMENTAL AND THEORETICAL METHODS

SnO_2 Synthesis and Characterization. Nanocrystalline SnO_2 was prepared by precipitation from aqueous solution of $SnCl_4$, obtained by dissolving 0.01 mol of $SnCl_4 \cdot 5H_2O$ in 90 mL of MilliQ. Then, 210 mL of a 0.33 M urea aqueous solution was added. All reagents were purchased at analytical grade from Sigma-Aldrich and were used without further purification. The reaction mixture was stirred for 8 h at 90 °C and then overnight at room temperature. The resulting precipitate was washed by centrifugation−resuspension cycles with water/ethanol. It was then suspended in water and treated in a Teflon-lined autoclave for 4 h at 130 °C. The powder was then dried in an oven at 80 °C and calcined for 6 h at 400 °C under O_2 flux.

The X-ray powder diffraction (XRPD) pattern was recorded using a Bruker D8 Advance diffractometer in Bragg−Brentano configuration, equipped with a Cu anticathode (Cu Kα, $\lambda \approx$ 1.54 Å). The sample specific surface area was determined from N_2 adsorption−desorption isotherms in subcritical conditions (Coulter SA 3100) according to the Brunauer−Emmett−Teller (BET) method. Fourier transform infrared (FTIR) spectra were recorded on the as-synthesized sample using a Perkin Elmer Spectrum 100 spectrophotometer working in attenuated total reflectance (ATR) mode. Spectra were acquired using a resolution of 4.0 cm^{-1} and a total of 12 scans between 4000 and 400 cm^{-1}.

Thermogravimetric analysis (TGA) curves were acquired on a Mettler-Toledo TGA/DSC 3+ STAR System in the 30−900 °C range with a 5 °C min^{-1} heating rate under N_2 flux.

High-resolution transmission electron microscopy (HRTEM) images were obtained on a JEOL 3010−UHR instrument equipped with a LaB_6 filament (acceleration potential, 300 kV). All digital micrographs were acquired by an Ultrascan 1000 camera, and image processing was performed by a Gatan Digital Micrograph program version 3.11.1. Samples were dry dispersed onto Cu grids coated with a "lacey" carbon film before analysis.

Raman spectra were recorded on the plain powder by means of a Bruker Vertex 70 spectrometer, equipped with the RAMII

https://dx.doi.org/10.1021/acs.jpcc.0c02546
J. Phys. Chem. C 2020, 124, 14202−14212

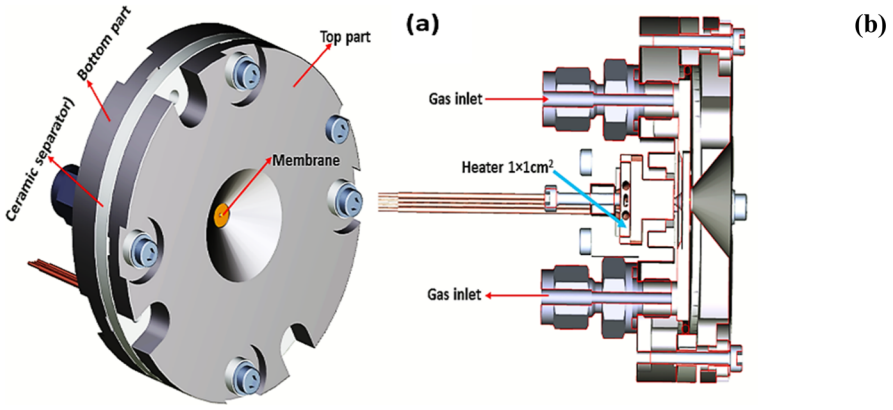

Figure 1. (a) 3D drawing of the front part of the reactor cell for ambient-pressure operando XAS experiments, as seen from the X-ray beam. The reactor cell contains a gas fluxing circuit and a Si_3N_4 membrane (window), of 100 nm thickness. The membrane separates the sample lodging, which is at ambient (1 atm) pressure, from the rest of the beamline, which is in high-vacuum conditions, permitting the transmission of the incident soft X-ray beam without significant loss of intensity in the photon energy range of interest. (b) Vertical section of the reactor cell in which the gas circuit, the heater, and the sample environment are clearly visible.

accessory and Ge detector, by exciting samples with a Nd:YAG laser source (1064 nm). Spectral resolution was 4 cm^{-1}.

XAS Experiment. To obtain high-quality in situ soft-XAS data, the reaction cell shown in Figure 1 was used.[36] The cell is installed at the advanced photoelectric effect high-energy (APE-HE) beamline at the ELETTRA synchrotron radiation source and can operate in the temperature range from RT to ca. 360 °C. The XAS detection in total electron yield (TEY) mode was achieved by measuring the drain current from the sample with a picoammeter. The monochromator of the APE-HE beamline allows continuous scanning of the X-ray energies; this, combined with the high signal-to-noise ratio of TEY, makes it possible to record XAS spectra in very short times, of the order of few seconds. For the XAS experiment, a small amount of the SnO_2 nanoparticles (5 mg ca.), in the form of loose powder, was hand-pressed on the sample holder of the reaction cell of the APE beamline at the ELETTRA synchrotron radiation facility. The sample holder is fixed with screws onto the titanium base of the cell, which is floating from the ground and connected with a coaxial cable. In this geometry, the X-ray beam passes through the membrane and the gas layer then hits the sample and generates the secondary emission, which is collected by a picoammeter connected to the sample and measuring the drain current. All measurements were performed by keeping the sample grounded through the picoammeter and applying a positive bias voltage of 40 V to the membrane. The cell is mounted in the ultrahigh-vacuum chamber of the APE-HE beamline, coaxially with the X-ray beam. The reaction cell was mounted on an *x*-*y* table that allows its movement in the plane perpendicular to the incident beam with 5 μm vectorial precision. This allows the alignment of the membrane onto the beam. The sample surface, inside the cell, sits on the focal point of the beamline. The measurements were performed at the O K-edge, between 528 and 547 eV, and at the Sn $M_{4,5}$-edges, between 480 and 510 eV, at different temperatures and under a total pressure of 1 bar. To ensure maximum gas purity, especially concerning water and carbon oxides, the He carrier gas was passed through a liquid N_2 trap before entering the cell. The spectra at both edges have been background-subtracted by fitting the pre-edge with a straight line. The spectra at the Sn $M_{4,5}$-edges ere normalized at unit absorption at 508 eV. The spectra at the O K-edge are shown without further manipulation, except in cases where it is explicitly stated differently.

Theoretical Calculations. DFT calculations were performed for water-loaded $SnO_2(110)$ interfaces with the Vienna ab initio simulation package (VASP 5.4.1)[37,38] using the GGA approach. The PBE exchange-correlation was applied.[39,40] To include van der Waals interactions, the dDsC dispersion correction method is employed (PBE-dDsC).[41−43] The projector augmented wave approximation (PAW)[44] is used to describe the interaction between the valence electrons and the atom cores. Sn and O were treated with 4 and 6 electrons in the valence, respectively. Bulk SnO_2 was optimized using a plane wave kinetic energy cutoff of 1000 eV and a Γ-centered *k* point grid of at least 12 × 12 × 12. For SnO_2, the optimized cell parameters are ($a = b$), 4.82 Å in the *a*- and *b*-direction and 3.24 Å in the *c*-direction, respectively. Subsequently, a 4-layered (4×4) slab is constructed with $SnO_2(110)$ termination at the top and bottom of the *z*-direction (Supporting Information, Figure S1). On such slabs, water chemisorption and the fate of methane are studied. All bulk $SnO_2(110)$ slabs were structurally relaxed using a plane wave cutoff energy of 450 eV, and Brillouin zone sampling was restricted to the Γ-point. A Gaussian smearing[45] of 0.05 eV was applied to improve convergence. Additionally, the convergence criterion for the electronic self-consistent field (SCF) problem is set to 10^{-5} eV for cell optimizations, and structures are relaxed until all forces are below 0.03 eV/Å. A vacuum of at least 18 Å in the *z*-direction is present for all optimized models.

Ab initio thermodynamics is used to calculate adsorption/desorption equilibria (Figure 5c) or construct phase diagrams ranking different hydrated $SnO_2(110)$ surface slabs (see Figure S7). The pressure and temperature dependence of the equilibrium is introduced via chemical potential of the species in the gas phase. For example, for a compound C, which can adsorb and desorb from a SnO_2 surface slab, this can be written as follows

$$\Delta G(T,p) = (G^{\mathrm{slab}}_{SnO_2,C(ads)}(T,p) - G^{\mathrm{slab}}_{SnO_2}(T,p) - \mu_c(T,p)) \approx (E^{\mathrm{slab}}_{SnO_2,C(ads)} - E^{\mathrm{slab}}_{SnO_2} - \mu_c(T,p)) \quad (1)$$

In these equations, we can approximate the free-energy difference with and without adsorbed species C with the zero-point corrected energy difference ($G = E + PV - TS \approx E$).

https://dx.doi.org/10.1021/acs.jpcc.0c02546
J. Phys. Chem. C 2020, 124, 14202−14212

Then, we neglect the PV term as well as the TS term for the surface slabs. The chemical potential of species C can be written as the following sum

$$\mu_c(T, p) = E_C^{tot} + \Delta\mu_O(T, p) = E_C^{tot} + \Delta\mu_C(T, p^0) + k_B T \ln\left(\frac{p}{p^0}\right) \quad (2)$$

Here, E_C^{tot} represents the zero-point corrected energy, while $\Delta\mu_C(T, p)$ can be calculated via the tabulated standard chemical potentials $\Delta\mu_C(T, p^0)$ at p^0=1 bar.[46] The standard chemical potentials $\Delta\mu(T, p^0)$ at p^0= 1 bar can be calculated from enthalpy and entropy; for example

$$\Delta\mu_{H_2O}(T, p^0) = (H(T, p^0, H_2O) - H(0\ K, p^0, H_2O)) - T(S(T, p^0, H_2O) - S(0\ K, p^0, H_2O)) \quad (3)$$

Equilibria between adsorption and desorption can then be approximately calculated from eq 1 assuming $\Delta G(T, p) = 0$ and visualized in a (T,p) diagram.

RESULTS AND DISCUSSION

Sample Characterization. The SnO_2 nanoparticles were prepared as described in the method section. The phase purity of the nanoparticles was checked before the XAS experiment by means of X-ray powder diffraction. The pattern (Figure S2, Supporting Information) shows the characteristic reflections of cassiterite SnO_2 only. The crystallite size was estimated according to the Scherrer equation, showing an average grain dimension of 3.5 nm. The specific surface area, measured as described in the materials and methods' section, is 117 $m^2\ g^{-1}$; considering the average grain size and assuming particles with a spherical shape and cassiterite bulk density, the surface area value is indicative of a high degree of aggregation.

Notwithstanding the assumptions made in this estimate, the aggregation is independently confirmed by HRTEM results as shown in Figure S3, where a representative HRTEM image of the as-prepared SnO_2 sample is shown. The oxide particles are indeed highly agglomerated, as individual objects cannot always be singled out. Almost all particles exhibit roundish contours, and the average particle size can be estimated (assuming an almost spherical form or, at least, a pebble-like shape) to be in the 3−5 nm range, in excellent agreement with the XRPD results, thus allowing the definition of nanoparticles. Moreover, the SnO_2 nanoparticles are very thin (supporting then a pebble-like shape) and closely packed, giving rise to frequent fringe patterns, either "normal" and due to thickness or of a Moiré character. The analysis of both fringes and fast Fourier transform (FFT) patterns of the fringes themselves (Figure S3 inset) confirms the presence of the crystallographic planes belonging to the (110) of cassiterite with $d_{(hkl)}$ = 0.33 nm (ICDD card no. 01-071-0652). The feature was revealed (i) onto many different portions of the sample and (ii) for many different parts of the sample.

The single phase of the nanoparticles is confirmed by the Raman spectrum reported in Figure S4. The spectrum is dominated by a sharp and intense component at ∼630 cm^{-1}, in addition to two minor spectral components at ∼475 cm^{-1} (sharp, but with low intensity) and at ∼725 cm^{-1} (broad and low in intensity). All observed components can be ascribed, on the basis of both their spectral features and literature data,[47] to SnO_2 Raman modes. In particular, components at 630, 475, and 725 cm^{-1} can be attributed to the A_{1g}, E_g, and B_{2g} vibrational modes, respectively. As the Raman spectrum becomes totally opaque in the high-frequency region, no other spectral components could be singled out.

The FTIR spectrum of the as-synthesized SnO_2 sample (Figure S5, Supporting Information) shows as the main feature a broad band in the 700−400 cm^{-1} region, which is attributed to Sn−O and Sn−O−Sn stretching vibrations.[48] Moreover, a broad band in the 3700−3000 cm^{-1} range is attributed to stretching vibrations of hydroxyl groups and physisorbed water, mutually interacting by hydrogen bonding. The corresponding bending counterpart can be appreciated at 1640 cm^{-1}. It should be noted that FTIR spectra were recorded on the as-synthesized powder, and hence, the presence of abundant surface hydration might cover any signals of free OH groups. No peaks characteristic of organic contaminants (e.g., CH_x or C═O stretching vibrations) can be observed. Thermogravimetric analysis (TGA, Figure S6, Supporting Information) shows a loss of physisorbed water at T < 100 °C and a broader feature starting at about 400 °C accounting for an overall weight loss of about 4%; the latter can be related, in agreement with FTIR results and previous literature, mainly to the loss of chemisorbed water.[49] As a result, an average surface density of ca. 5 OH groups per nm^2 can be estimated,[50] which is in good agreement with previous studies.[49] It should be noted that TGA shows that in the temperature range between 100 and 360 °C, the weight loss is the smallest, amounting to ca. 0.1%. To better understand this fact, DFT calculations of adsorption energy were performed. We found that on the bare SnO_2(110), water can be adsorbed dissociatively (Figure S7, Supporting Information), with an average chemisorption energy of −161.6 kJ/mol (PBE-dDsC) per water molecule (at PBE, −140.1 kJ/mol). The first H_2O molecule chemisorbs strongly onto our bare SnO_2(110) model system, with a reaction energy of −164.9 kJ/mol (θ_{H_2O}:0 → 1/8, where θ_{H_2O} is the coverage degree). The chemisorption energy of the last molecule is −159.9 kJ/mol (θ_{H_2O}:7/8 → 8/8). There is thus about 5 kJ/mol difference between the first and the last H_2O during chemisorption, and the average chemisorption energy of 8 water molecules lies in between (−161.7 kJ/mol).

More loosely bound water (physisorbed water) can further adsorb on the SnO_2(110) already covered with chemisorbed water, with adsorption energies of −78.0 kJ/mol (PBE-dDsC, at PBE; −60.8 kJ/mol) for the first layer and −49.6 kJ/mol (PBE-dDsC, at PBE; −33.6 kJ/mol) for the second layer (Figure S7), characteristic of hydrogen-bonded water. These different adsorption energies are closely reflected in the TGA curve: The weight loss for T < 100 °C is associated to the first and second layer of physisorbed water (and additional layers); above 100 °C, the weight loss is associated with the desorption of chemisorbed water, which happens at a much slower rate in the TGA in the 100 < T < 360 °C range.

Operando Soft-XAS Experiment. The XAS experiment was performed at the O K- and Sn $M_{4,5}$-edges using the experimental ambient-pressure XAS cell shown in Figure 1.[36,51] In order to clean the sample surface from the physisorbed water, after being mounted in the reaction gas XAS cell, the sample was heated up to 300 °C in flowing He at 20 sccm and then cooled down to room temperature.

https://dx.doi.org/10.1021/acs.jpcc.0c02546
J. Phys. Chem. C 2020, 124, 14202−14212

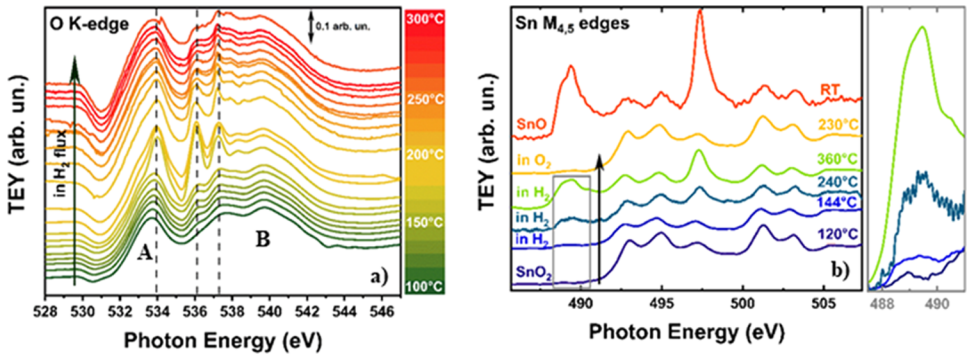

Figure 2. (a) Evolution of the O K-edge spectra of the SnO_2 nanoparticles in flowing H_2 as a function of temperature. The spectra are shifted along the *y* axis for the sake of better clarity. The vertical dotted lines mark the position of the main peaks of water in the gas phase. Peaks A and B are the main peaks of SnO_2, whose origin is described in the text. (b) Sn $M_{4,5}$-edges of the SnO_2 nanoparticles at different temperatures and in different conditions. The spectrum of standard SnO is shown for reference, and the spectra are shifted along the *y* axis as in a. The spectrum after the reoxidation in O_2 at 230 °C is also shown as a yellow line. The region between 487.5 and 492 eV for the SnO_2 nanoparticles at 120, 144, 240, and 360 °C in H_2 is evidenced for better reference.

Figure S8 (Supporting Information) compares the spectra obtained for the sample as it is and during the initial thermal treatment; that obtained in vacuum conditions is also shown for better reference.

The peak at ca. 531 eV is due to molecular oxygen (see Figure S9, Supporting Information), and it is reasonably due to desorption from the gas pipeline. The dip at ca. 531 eV is due to small oxygen impurities in the beamline, and it is better discussed in the Supporting Information (Figure S8); here, we note that it can be safely ignored. Between 533 and 543 eV, the spectra at $T > 100$ °C show a series of features. In particular, the peaks at ca. 534, 536.1, and 537.2 eV are due to the appearance of molecular water in the gas phase, confirming that in the temperature range $100 < T < 300$ °C, the desorption of physisorbed water takes place. Comparing the spectrum obtained at room temperature, in flowing He and after this thermal treatment, with that obtained in rough vacuum (10^{-3} torr) before the thermal treatment demonstrates that SnO_2 is now free of physisorbed water, in agreement with the TGA measurements. However, TG and DFT calculation show that dissociatively chemisorbed water is still present at the surface, and therefore, the SnO_2 nanoparticles are terminated by hydroxyl groups. For the sake of conciseness, in the following, this will be referred to as the "clean SnO_2 surface". In addition, the spectrum in rough vacuum shows again a small peak between 530 and 531.5 eV due to desorption of O_2 from the cell pipeline, demonstrating the sensitivity of the O K-edge spectra to small amounts of oxygen-containing species in the gas phase. It is also noted that comparison with literature data shows a small broadening of the spectral features at the O K-edge of the SnO_2 sample when compared to literature data.[52] This may be caused by the large amount of uncoordinated atoms that are present at the surface due to the nanosize of our sample.

The sample was then heated while flowing a mixture of He (20 sccm) and H_2 (5 sccm). The results are shown in Figure 2a (O K-edge) and b (Sn $M_{4,5}$-edges).

Due to the 1s character of the initial state, at the O K-edge, the $\Delta l = \pm 1$ dipole selection rule allows transition to empty states with the p character only. In addition, the localized nature of the core hole in the 1s orbital that is formed after photon absorption projects the density of the final states onto states with the O character only.[53] The two intense peaks in the O K edge spectrum are then due to transitions to O 2p states hybridized with Sn 5s states at the bottom of the conduction band (peak A in Figure 2a) and to transition to antibonding O 2p states hybridized with Sn 5s and 5p states in the conduction band (peak B in Figure 2a), respectively.[52] According to the same type of considerations, the final states at the Sn $M_{4,5}$-edges are of Sn p and f character, with the spin−orbit coupling splitting the initial states in $3d_{3/2}$ (M_4) and $3d_{3/2}$ (M_5), respectively. The Sn $M_{4,5}$-edge spectrum then maps the PDOS of the empty Sn 5p and 5f character in the conduction band.[53]

At 100 °C, the O K-edge spectrum shows a close resemblance with that of a clean SnO_2 nanoparticle surface. Above this temperature, some additional peaks at ca. 534, 536.1, and 537.2 eV start to appear, with increasing intensity with increasing *T*. These peaks are strictly corresponding to that of H_2O in the gas phase (Figure S9). In this case, we start with a clean surface, without physisorbed water, and in this temperature range, where we demonstrated that desorption of chemisorbed water cannot occur, these additional peaks can only be attributed to a reduction by H_2 of the SnO_2 surface to produce water in the gas phase. To further investigate this point, a spectrum at the Sn $M_{4,5}$-edges was acquired in flowing H_2 at ca. 144 °C. A close inspection of this spectrum in the region between 487.5 and 492 eV (inset in Figure 2b) shows the presence of an additional peak, which, by comparison with the spectrum of reference SnO, can only be attributed to the formation of Sn(II), thus confirming the reduction (see Table S1 in the Supporting Information).

At the O K-edge, the additional peaks at ca. 534, 536.1, and 537.2 eV show a sudden and dramatic boost at ca. 190 °C, showing that the rate of the reaction producing water becomes conspicuous. Then, a striking decrease of water production is found for $T > 240$ °C. Simultaneously, the Sn $M_{4,5}$-edge data in Figure 2b show a noticeable increase of the extra peak at ca. 489 eV and an increase in intensity of the peak at 497.5 eV, both due to the formation of an increased amount of Sn(II). At ca. 240 °C, the spectrum at the Sn $M_{4,5}$-edges shows that the reduction of SnO_2 goes well beyond the surface, and a further increase of the reduction is found at 360 °C. A quantification of the thickness of the SnO layer can be obtained by measuring the area of the peak at 489 eV, which is only due to Sn(II), normalized by the area of the peaks at 492.5 and 494.5, which are almost only due to Sn(IV) (see Figure S10, Supporting Information). Taking into account that the mean probing

https://dx.doi.org/10.1021/acs.jpcc.0c02546
J. Phys. Chem. C 2020, 124, 14202−14212

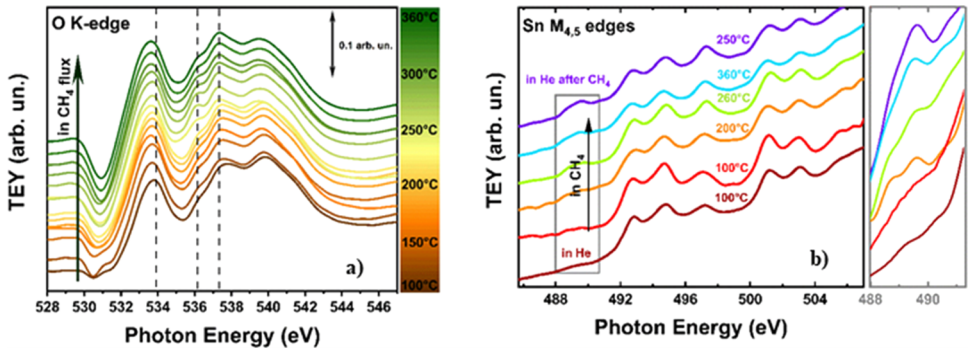

Figure 3. (a) Evolution of the O K-edge spectra of the SnO_2 nanoparticles in flowing CH_4 as a function of temperature. As in Figure 1, the spectra are shifted along the *y* axis for the sake of better clarity, and the vertical dotted lines mark the position of the main peaks of water in the gas phase. (b) Sn $M_{4,5}$-edges of the SnO_2 nanoparticles at different temperatures in flowing CH_4. The spectra are shifted along the *y* axis as in a. The increase of the Sn(II) signature at 489 eV is shown on an enlarged scale for better reference.

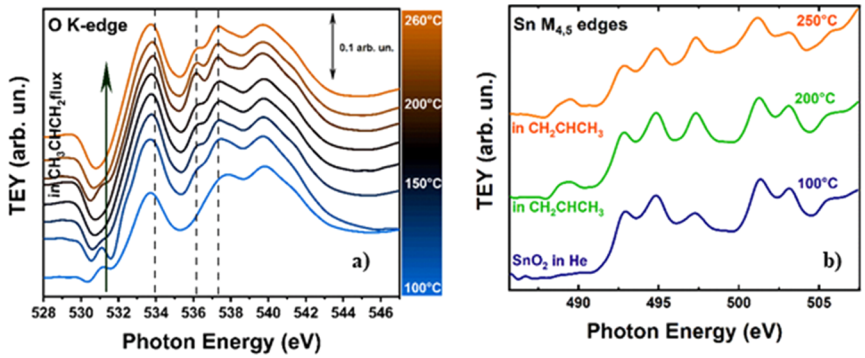

Figure 4. (a) Evolution of the O K-edge spectra of the SnO_2 nanoparticles in flowing CH_2CHCH_3 as a function of temperature. As in Figure 1, the spectra are shifted along the *y* axis for the sake of better clarity, and the vertical dotted lines mark the position of the main peaks of water in the gas phase. (b) Sn $M_{4,5}$-edges of the SnO_2 nanoparticles at different temperatures in flowing CH_2CHCH_3. The spectra are shifted along the *y* axis as in a.

depth λ of electrons in the total electron yield at 500 eV amounts to ca. 3.5 nm,[54] the thickness of the reduced layer at 360 °C is ca. 1.5(5) nm, which corresponds to a width of at least 3−4 unit cells. This surface layer prevents further reduction of the SnO_2 nanoparticles and avoids further production of water. Notably, as it is shown in Figure 2b, the reduction can be fully reversed by flowing O_2 in the ambient-pressure XAS cell at T > 200 °C. The Sn $M_{4,5}$-edge spectrum obtained after this treatment shows that the spectral shape of SnO_2 is fully recovered. To further confirm that H_2O is present in the gas phase, we fitted the spectrum at 200 °C at the O K edge with a linear combination of the spectra of water in the gas phase and of the SnO_2 nanoparticles in vacuum. The agreement, as shown in Figure S11 of the Supporting Information, is rather satisfactory.

After having demonstrated that in situ soft-XAS is successful (in real working conditions) in both detecting gas products of surface reaction(s) and the variations in the Sn oxidation state at the surface produced by these reaction(s), we consider the effects of hydrocarbons like CH_4 and CH_2CHCH_3.

Experiments with methane (He (20 sccm) + CH_4 (5 sccm)) were conducted in the 100 ≤ T ≤ 360 °C temperature range. Before running the experiments, the sample was fully oxidized as described above. The results at the O K-edge are shown in Figure 3a. At 100 °C, the O K edge spectrum corresponds to a clean SnO_2 surface, free of physisorbed water. This is again in agreement with the TGA measurements of Figure S6, showing that the rate of water desorption is minimum in the 100 ≤ T ≤ 360 °C temperature range. At T = 120 °C, the CH_4 flux produces an appearance of the signatures of water in the gas phase.

These signatures show an increase at T ≥ 240 °C, with a maximum at 310 °C, and then a decrease when going from 310 to 360 °C. The spectra at the Sn $M_{4,5}$-edges are shown in Figure 3b. Here, we note that signatures of Sn(II) start to appear after the treatment in CH_4 at T = 120 °C, with an intensity that is increasing by increasing T, as it is shown by the inset in Figure 3b.

Results with CH_2CHCH_3 (He (20 sccm) + CH_2CHCH_3 (5 sccm)) are analogous. Also in this case, before running the experiment, the sample was fully oxidized by flowing O_2 at 200 °C. The measurements were performed in the 100 ≤ T ≤ 260 °C temperature range. The pertinent spectra at the O K-edge are shown in Figure 4a. Again, we observe that the initial conditions correspond to that of an almost clean SnO_2 and that the signatures of water in the gas phase appear for T ≥ 120 °C, reaching a maximum at 200 °C and then decreasing at higher temperatures. The spectral intensity of the water peaks is larger for propylene than for methane, in agreement with the higher reactivity of propylene. Again, at the Sn $M_{4,5}$-edges (Figure 4b), the hydrocarbon flow induces an appearance of the peaks of Sn(II).

An important point to note is that with both methane and propylene, signatures of carbon oxides are never detected by soft-XAS, even if the spectra of both CO and CO_2 show very large pre-edge peaks at the O K-edge[55] that are likely to show up in the spectra (see Figure S9), even if these compounds are present in very low concentrations. It is also noted that the

https://dx.doi.org/10.1021/acs.jpcc.0c02546
J. Phys. Chem. C 2020, 124, 14202−14212

cross section of CO and CO_2 at the O K-edge is at least five times larger than that of water,[56,57] indicating that the possible formation of carbon oxides is well within the sensitivity of our soft-XAS experiment. The non-appearance of carbon oxide in the O K-edge spectra has the obvious meaning that hydrocarbons react with the clean SnO_2 surface by directly providing electrons rather than by removing surface-oxygenated species. Likely, SnO_2 behaves in these cases like an electron sponge, being able to easily accept and return electrons depending on the gas species that are close to the surface. This is also confirmed by the ease with which the reduced surface can be restored in its fully oxidized form. The electrons provided by reducing gases localize on Sn to form Sn(II) and eventually an SnO layer at the surface. Quantification of the thickness of the SnO layer using the same method described above for the reduction with H_2 gives a figure of 0.6(2) nm at 360 °C in CH_4 and 0.5(2) nm at 250 °C in CH_2CHCH_3 (see Figure S10, Supporting Information), which correspond to a width of 1−2 SnO_2 unit cells in both cases. The thicknesses in CH_4 and CH_2CHCH_3 are comparable despite the fact that the reduction is faster in CH_2CHCH_3 because the SnO_2 nanoparticles have been exposed to methane at high T for a longer time.

DFT Calculations. Experimental evidence described above allowed us to propose different dissociative hydrocarbon routes that have been tested by DFT calculations. For the sake of simplicity but without any loss of generality, we studied the dissociative adsorption of CH_4 on fully hydroxylated $SnO_2(110)$ surfaces ($\theta_{H_2O} = 1$), mimicking the predominantly exposed clean surface in the experiments (Figures 5 and 6). These (110) surfaces consist of Sn^{4+} and have both dangling Sn−OH and bridged Sn−OH−Sn groups (Figure 5). Furthermore, they are fully H-saturated, and therefore, the reaction with CH_4 takes place via physisorption of CH_4 (−19.2 kJ/mol) followed by C−H cleavage forming adsorbed CH_3OH. Here, two different reaction possibilities are tested, forming the adsorbed CH_3OH either via CH_3 addition to a dangling Sn−OH bond or to a bridged Sn−OH−Sn bond, represented in Figures 5 and 6, respectively. The most stable reorganized structures after O−CH_3 bond formation are at −114.7 and −102.3 kJ/mol (see Figures 5 and 6). From these states, the desorption of CH_3OH and H_2O was considered. This means that when the adsorption energy is similar, CH_3OH desorption from the $SnO_2(110)$ surface takes place at higher temperatures compared to H_2O. In the case of water, we find desorption energies of 124 and 111 kJ/mol (see Figures 5 and 6). Within experiment, it is clear that H_2O formation happens from 100 °C after exposure of the SnO_2 nanoparticles to CH_4 (see Figure 2), and this agrees with the computational result that reaction with CH_4 lowers the H_2O adsorption energies (Figures 5 and 6). In particular the adsorption energy is lowered from strongly chemisorbed H_2O (−161.6 kJ/mol) to physisorbed H_2O (−124 and −111 kJ/mol), making it easier for H_2O to desorb.

To estimate the feasibility of C−H activation on fully hydrated SnO_2, we can use the Evans−Polanyi principle, stating that there is a relationship between the activation energy and the energy of formation, and comparisons can be made with similar reactions. Such relationships for CH_4 activation are universal for different materials, e.g., oxides, zeolites, MOFs, etc. and have been determined computationally via screening of various materials.[58] In particular, if the

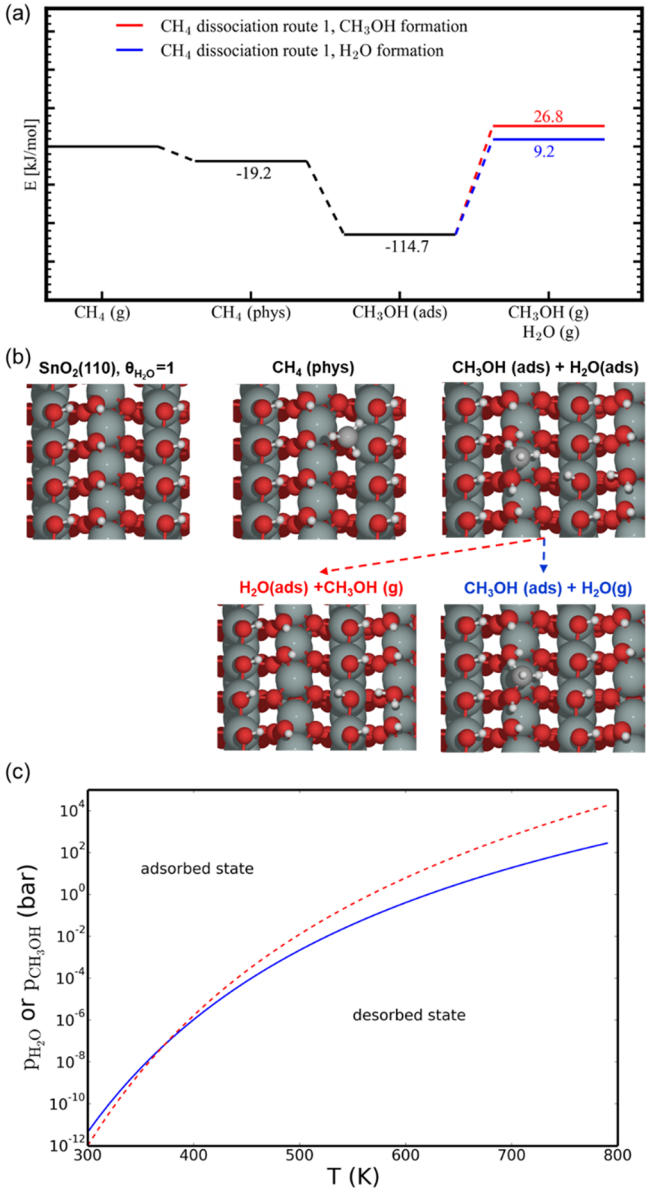

Figure 5. (a) Energy diagram for the production of CH_3OH and H_2O from CH_4 on a fully hydroxylated $SnO_2(110)$ surface via CH_3 deposition on a dangling Sn−OH bond forming adsorbed (ads) CH_3OH and (b) schematic representation of the different states of $SnO_2(110)$ in the above energy diagram (a). Color code: Sn (green), O (red), C (gray), and H (white). (c) Calculated adsorption/desorption equilibrium curves for H_2O (blue) and CH_3OH (red).

transition state (TS) has a radical character, the activation barrier relates to the hydrogen adsorption energy via the relationship $E_{TS} = 0.75E_H + 1.09$ [eV], and E_H is calculated based on the energy difference of the active site before and after hydrogenation in the case of an oxide

$$E_H = E(M_mO_xH_{y+1}) - E(M_mO_xH_y) - \frac{1}{2}E(H_2O) + \frac{1}{4}E(O_2) \quad (4)$$

Using this formula and scaling relations, we can estimate the reaction barrier for CH_4 activation via a radical-like intermediate. For the fully hydrated $SnO_2(110)$ model with chemisorbed H_2O ($\theta_{H_2O} = 1$), we identified reaction barriers of

https://dx.doi.org/10.1021/acs.jpcc.0c02546
J. Phys. Chem. C 2020, 124, 14202−14212

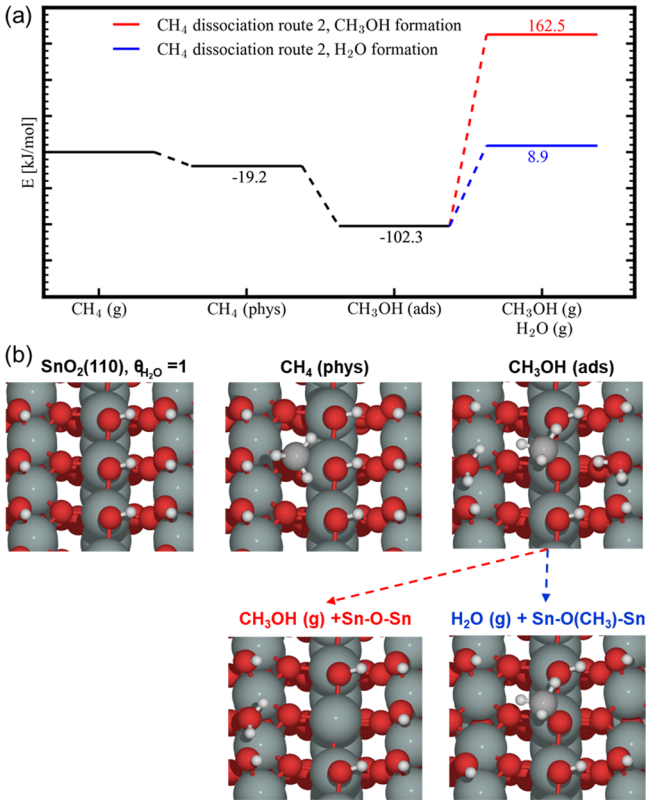

Figure 6. (a) Energy diagram for the production of CH_3OH and H_2O from CH_4 on a fully hydroxylated $SnO_2(110)$ surface via CH_3 deposition on a Sn−O−Sn bridge forming adsorbed (ads) CH_3OH and (b) schematic representation of the different states of $SnO_2(110)$ in the above energy diagram (a). Color code: Sn (green), O (red), C (gray), and H (white).

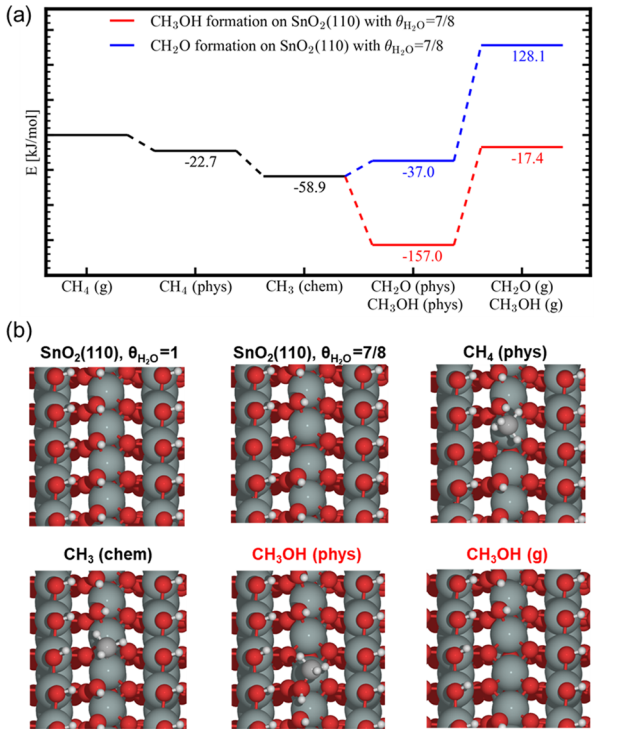

Figure 7. (a) Energy diagram for the production of CH_3OH or CH_2O from CH_4 on a hydroxylated $SnO_2(110)$ surface (H_2O coverage of 7/8) via CH_3 chemisorption (chem) on the bare Sn site followed by the formation of physisorbed (phys) CH_3OH or CH_2O and (b) schematic representation of the different states of $SnO_2(110)$ in the above energy diagram (a). In this case, the formation of H_2O from the physisorbed CH_3OH state is more endothermic than the formation of gas-phase CH_3OH (energy level, −13.1 kJ/mol). Color code: Sn (green), O (red), C (gray), and H (white).

about 110.7 ± 1.1 kJ/mol. These are realistic reaction barriers resulting in feasible turnover rates at higher temperatures (>150 °C). Methanol probably reacts further on the surface as it is not observed in the products.

In another scenario we investigated, the $SnO_2(110)$ surface is not fully hydroxylated, and therefore, one water molecule was removed (θ_{H_2O} = 7/8), creating a free Sn site and an O site without hydrogen (Figure 7). In this case, methane is slightly exothermically physisorbed at the free Sn site. The nearby oxygen removes a hydrogen, and the remaining $-CH_3$ group becomes chemisorbed, forming a Sn−CH_3 bond. This step is exothermic with about 59 kJ/mol compared with methane in the gas phase. In the next step, a methoxy group is formed, and water leaves the surface, reforming a free Sn site.

This reaction is exothermic with −157 kJ/mol and shows that the CH_3OH group is strongly physisorbed onto the surface. Since the active site is reformed, the reaction is autocatalytic and will stop once all available sites are sterically blocked by methanol or methoxy groups.

These results clearly show that both water and methanol cannot be formed unless the desorption energies are lowered further, for example, via extra surface reactions with CH_4. Remark that as soon as bond-deficient Sn sites at the surface are formed, species like Sn−CH_3 can appear at the surface. Through such an electron-rich covalent bond, surface Sn(IV) gets eventually reduced. The fact that a Sn(II) signature is observed and that only 1−2 layers of SnO were found experimentally further support this latter reaction sequence.

The results described above can be further discussed in the framework of the gas sensing mechanisms by SnO_2 proposed in the literature. The sensor response is explained by changes of the electric surface potential resulting from "ionosorption" of gaseous molecules (ionosorption model) or by changes in the oxygen stoichiometry, that is, by the variation of the number of (sub) surface oxygen vacancies and their ionization (reduction−reoxidation mechanism).[13] A very recent work concerning the mechanisms of gas sensing toward ethanol by SnO_2 concluded that the response is correlated with the number of oxygen vacancies, the nature of the adsorbates, and the presence of surface hydroxyl groups, thus supporting the reduction−reoxidation mechanism.[59] The present work makes a further step forward in this direction: Reducing gases such as hydrocarbons can directly provide electrons to SnO_2 nanoparticles via cleavage of the C−H bond(s). These electrons are at least partially localized on Sn to produce Sn(II); the reduced layer eventually forms a monolayer (or a couple of monolayers) of SnO at the surface. In principle, in this mechanism, the presence of oxygen vacant sites at the surface is not required. On the contrary, our results show that the presence of hydroxyl species is decisive for the dissociative chemisorption of hydrocarbons.

CONCLUSIONS

In conclusion, it is demonstrated that soft-XAS can be used to probe, in the same experiment, the products of a surface heterogeneous reaction both in the gas phase and, simulta-

https://dx.doi.org/10.1021/acs.jpcc.0c02546
J. Phys. Chem. C 2020, 124, 14202−14212

neously, on the surface. In particular, we experimentally demonstrated that reducing gases directly react with the hydroxylated SnO_2 surface, removing water and reducing Sn(IV) to Sn(II). The reduction is larger for H_2 than for hydrocarbons and is larger for unsaturated hydrocarbons than for alkanes. Hydrocarbons act as a reducing agent without the production of carbon oxides. This fact indicates that methoxy- or methyl-like species at the surface can be formed, as indicated by detailed theoretical DFT investigation on the reaction mechanism for the reduction with CH_4. As schematically represented in Figures 5−7, the surface reaction involves cleavage of the C−H bond of the incoming gas and subsequent reaction with OH groups on the surface to form H_2O and methoxy- or methyl-tin species on the surface. Because of this reduction, more loosely bound or physisorbed H_2O is formed, eventually leaving the SnO_2 surface. All data presented in this work reveal that the hydroxyl groups that are present at the SnO_2 surface play a crucial role in the adsorption properties: This evidence can be the basis for a better understanding of both sensing and catalytic properties of SnO_2 and, more generally, of oxide-based materials.

A final comment is due concerning the transferability of the present results to other systems. With a typical setup used at a synchrotron radiation beamline for the O K-edge, all edges within the 300 and 1200 eV energy range can be reached. This means that (i) all $L_{2,3}$ edges of the 3d transition metals, (ii) all $M_{2,3}$ edges of the 4d transition metals, (iii) all $N_{2,3}$ edges of the 5d transition metals, and (iv) the $M_{4,5}$-edges of the lanthanides from Ce to Tb can be probed in the same experiment. Although these are just few illustrations among the variety of edges that can be probed simultaneously with the O K-edge, these examples show that the methodology here described can in principle be applied to the vast majority of cases that are of interest when a solid is put in contact with a gas phase.

■ ASSOCIATED CONTENT

Supporting Information

The Supporting Information is available free of charge at https://pubs.acs.org/doi/10.1021/acs.jpcc.0c02546.

(Figures S1−S11) Chosen SnO_2(110) model system; XRD pattern; HRTEM; Raman and FTIR spectra of the SnO_2 nanoparticles; TGA curve; water loadings for SnO_2 in the DFT model; XAS spectra under the heating process; XAS spectra of the gaseous species relevant to the work; quantification of the reduced SnO_2 layer under the reducing gases; fitting of the O K-edge spectrum at 200 °C under H_2; (Table S1) peak assignment at the Sn $M_{4,5}$-edges (PDF)

■ AUTHOR INFORMATION

Corresponding Authors

Paolo Ghigna − *Dipartimento di Chimica, Università di Pavia, I-27100 Pavia, Italy; INSTM, Consorzio Interuniversitario per la Scienza e Tecnologia dei Materiali, 50121 Firenze, Italy;* orcid.org/0000-0002-8680-7272; Phone: +390382987574; Email: paolo.ghigna@unipv.it; Fax: +390382987575

Alessandro Minguzzi − *Dipartimento di Chimica, Università degli Studi di Milano, 20133 Milan, Italy; INSTM, Consorzio Interuniversitario per la Scienza e Tecnologia dei Materiali, 50121 Firenze, Italy;* orcid.org/0000-0002-8130-4465; Email: alessandro.minguzzi@unimi.it

Matthias Vandichel − *Department of Chemical Sciences and Bernal Institute, Limerick University, V94 T9PX Limerick, Ireland;* orcid.org/0000-0003-1592-0726; Email: matthias.vandichel@ul.ie

Authors

Luca Braglia − *CNR- Istituto Officina dei Materiali, 34149 Trieste, Italia;* orcid.org/0000-0003-0796-3670

Martina Fracchia − *Dipartimento di Chimica, Università di Pavia, I-27100 Pavia, Italy;* orcid.org/0000-0001-5366-153X

Daniela Meroni − *Dipartimento di Chimica, Università degli Studi di Milano, 20133 Milan, Italy; INSTM, Consorzio Interuniversitario per la Scienza e Tecnologia dei Materiali, 50121 Firenze, Italy;* orcid.org/0000-0002-3386-9293

Raju Edla − *CNR- Istituto Officina dei Materiali, 34149 Trieste, Italia;* orcid.org/0000-0003-4132-8259

Elisabet Ahlberg − *Department of Chemistry and Molecular Biology, University of Gothenburg, SE-412 96 Gothenburg, Sweden;* orcid.org/0000-0002-4946-4979

Giuseppina Cerrato − *INSTM, Consorzio Interuniversitario per la Scienza e Tecnologia dei Materiali, 50121 Firenze, Italy; Department of Chemistry and NIST Interdipartimental Center, Università degli Studi di Torino, 10125 Torino, Italy*

Piero Torelli − *CNR- Istituto Officina dei Materiali, 34149 Trieste, Italia*

Complete contact information is available at: https://pubs.acs.org/10.1021/acs.jpcc.0c02546

Author Contributions

○L.B. and M.F. share the role of the first author.

Author Contributions

The manuscript was written through contributions of all authors. All authors have given approval to the final version of the manuscript.

Notes

The authors declare no competing financial interest.

■ ACKNOWLEDGMENTS

This work has been partially performed in the framework of the Nanoscience Foundry and Fine Analysis (NFFA-MIUR Italy Progetti Internazionali) project. The ELETTRA synchrotron radiation facility is thanked for provision of beamtime (exp. 20175162). The Italian Ministry of University and Research is acknowledged for financial support through the PRIN 2107 program (project 2017KKP5ZR). A.M. and D.M. gratefully thank the Università degli Studi di Milano for financial support by means of Piano di Sostegno alla ricerca−2015/2017-Linea 2, terzo rinnovo-2018. Finally, the authors would like to dedicate this paper to the late Prof. Carlo Lamberti.

■ REFERENCES

(1) Seiyama, T.; Kato, A.; Fujiishi, K.; Nagatani, M. A New Detector for Gaseous Components Using Semiconductive Thin Films. *Anal. Chem.* **1962**, *34*, 1502−1503.

(2) Yamazoe, N.; Miura, N. *Chemical Sensor Technology*, Vol. *4*; Yamauchi, S., Ed.; Kodansha-Elsevier: New York, 1992.

(3) Korotcenkov, G. Metal Oxides for Solid-State Gas Sensors: What Determines Our Choice? *Mater. Sci. Eng., B* **2007**, *139*, 1−23.

(4) Ihokura, K.; Watson, J. *The Stannic Oxide Gas Sensor Principles and Applications*; CRC Press: Boca Raton. FL, USA, 1994.

(5) Comini, E.; Baratto, C.; Faglia, G.; Ferroni, M.; Vomiero, A.; Sberveglieri, G. Quasi-One Dimensional Metal Oxide Semiconductors: Preparation, Characterization and Application as Chemical Sensors. *Prog. Mater. Sci.* **2009**, *54*, 1−67.
(6) Shimizu, Y.; Egashira, M. Basic Aspects and Challenges of Semiconductor Gas Sensors. *MRS Bull.* **1999**, *24*, 18−24.
(7) Gurlo, A.; Riedel, R. In Situ and Operando Spectroscopy for Assessing Mechanisms of Gas Sensing. *Angew. Chem., Int. Ed.* **2007**, *46*, 3826−3848.
(8) Williams, D. E. Semiconducting Oxides as Gas-Sensitive Resistors. *Sens. Actuators, B* **1999**, *57*, 1−16.
(9) Barsan, N.; Weimar, U. Conduction Model of Metal Oxide Gas Sensors. *J. Electroceram.* **2001**, *7*, 143−167.
(10) Gurlo, A. Interplay between O2 and SnO_2: Oxygen Ionosorption and Spectroscopic Evidence for Adsorbed Oxygen. *ChemPhysChem* **2006**, *7*, 2041−2052.
(11) Barsan, N.; Schweizer-Berberich, M.; Göpel, W. Fundamental and Practical Aspects in the Design of Nanoscaled SnO_2 Gas Sensors: A Status Report. *Fresenius' J. Anal. Chem.* **1999**, *365*, 287−304.
(12) Sberveglieri, G. *Gas Sensors*; Kluwer: Dordrecht, 1992.
(13) Gurlo, A. *Insights into the Mechanism of Gas Sensor Operation in Metal Oxide Nanomaterials for Chemical Sensors*; Springer: New York, 2013.
(14) Batzill, M.; Diebold, U. The Surface and Materials Science of Tin Oxide. *Prog. Surf. Sci.* **2005**, *79*, 47−154.
(15) Wang, D.; Chen, Y.; Liu, Z.; Li, L.; Shi, C.; Qin, H.; Hu, J. CO_2-Sensing Properties and Mechanism of Nano-SnO_2 Thick-Film Sensor. *Sens. Actuators, B* **2016**, *227*, 73−84.
(16) Bordiga, S.; Groppo, E.; Agostini, G.; van Bokhoven, J. A.; Lamberti, C. Reactivity of Surface Species in Heterogeneous Catalysts Probed by In Situ X-Ray Absorption Techniques. *Chem. Rev.* **2013**, *113*, 1736−1850.
(17) Minguzzi, A.; Ghigna, P. *X-Ray Absorption Spectroscopy in Electrochemistry*, Electroana; Bard, A. J.; Zoski, C., Eds.; CRC Press-Taylor and Francis group: Boca Raton, FL, USA, 2017.
(18) Minguzzi, A.; Lugaresi, O.; Achilli, E.; Locatelli, C.; Vertova, A.; Ghigna, P.; Rondinini, S. Observing the Oxidation State Turnover in Heterogeneous Iridium-Based Water Oxidation Catalysts. *Chem. Sci.* **2014**, *5*, 3591−3597.
(19) Minguzzi, A.; Locatelli, C.; Lugaresi, O.; Achilli, E.; Cappelletti, G.; Scavini, M.; Coduri, M.; Masala, P.; Sacchi, B.; Vertova, A.; Ghigna, P.; Rondinini, S. Easy Accommodation of Different Oxidation States in Iridium Oxide Nanoparticles with Different Hydration Degree as Water Oxidation Electrocatalysts. *ACS Catal.* **2015**, *5*, 5104−5115.
(20) Fracchia, M.; Ghigna, P.; Vertova, A.; Rondinini, S.; Minguzzi, A. Time-Resolved X-Ray Absorption Spectroscopy in (Photo)-Electrochemistry. *Surfaces* **2018**, *1*, 138−150.
(21) Velasco-Vélez, J. J.; Pfeifer, V.; Hävecker, M.; Wang, R.; Centeno, A.; Zurutuza, A.; Algara-Siller, G.; Stotz, E.; Skorupska, K.; Teschner, A.; et al. Atmospheric Pressure X-Ray Photoelectron Spectroscopy Apparatus: Bridging the Pressure Gap. *Rev. Sci. Instrum.* **2016**, *87*, 053121.
(22) Heine, C.; Hävecker, M.; Stotz, E.; Rosowski, F.; Knop-Gericke, A.; Trunschke, A.; Eichelbaum, M.; Schlögl, R. Ambient-Pressure Soft X-Ray Absorption Spectroscopy of a Catalyst Surface in Action: Closing the Pressure Gap in the Selective n-Butane Oxidation over Vanadyl Pyrophosphate. *J. Phys. Chem. C* **2014**, *118*, 20405−20412.
(23) Schwanke, C.; Xi, L.; Lange, K. M. A Soft XAS Transmission Cell for Operando Studies. *J. Synchrotron Radiat.* **2016**, *23*, 1390−1394.
(24) Xi, L.; Schwanke, C.; Xiao, J.; Abdi, F. F.; Zaharieva, I.; Lange, K. M. In Situ L-Edge XAS Study of a Manganese Oxide Water Oxidation Catalyst. *J. Phys. Chem. C* **2017**, *121*, 12003−12009.
(25) Jiang, P.; Chen, J.-L.; Borondics, F.; Glans, P.-A.; West, M. W.; Chang, C.-L.; Salmeron, M.; Guo, J. In Situ Soft X-Ray Absorption Spectroscopy Investigation of Electrochemical Corrosion of Copper in Aqueous $NaHCO_3$ Solution. *Electrochem. Commun.* **2010**, *12*, 820−822.
(26) Fracchia, M.; Ghigna, P.; Pozzi, T.; Anselmi Tamburini, U.; Colombo, V.; Braglia, L.; Torelli, P. Stabilization by Configurational Entropy of the Cu(II) Active Site during CO Oxidation on $Mg_{0.2}Co_{0.2}Ni_{0.2}Cu_{0.2}Zn_{0.2}O$. *J. Phys. Chem. Lett.* **2020**, 3589−3593.
(27) Tesch, M. F.; Bonke, S. A.; Jones, T. E.; Shaker, M. N.; Xiao, J.; Skorupska, K.; Mom, R.; Melder, J.; Kurz, P.; Knop-gericke, A.; et al. Evolution of Oxygen−Metal Electron Transfer and Metal Electronic States During Manganese Oxide Catalyzed Water Oxidation Revealed with In Situ Soft X-Ray Spectroscopy. *Angew. Chem., Int. Ed.* **2019**, *131*, 3464−3470.
(28) Edla, R.; Braglia, L.; Bonanni, V.; Miotello, A.; Rossi, G.; Torelli, P. Study of Gaseous Interactions on Co_3O4 Thin Film Coatings by Ambient Pressure Soft X-Ray Absorption Spectroscopy. *J. Phys. Chem. C* **2019**, *123*, 24511−24519.
(29) Mueller, D. N.; Machala, M. L.; Bluhm, H.; Chueh, W. C. Redox Activity of Surface Oxygen Anions in Oxygen-Deficient Perovskite Oxides during Electrochemical Reactions. *Nat. Commun.* **2015**, *6*, 1.
(30) Herranz, T.; Deng, X.; Cabot, A.; Guo, J.; Salmeron, M. Influence of the Cobalt Particle Size in the CO Hydrogenation Reaction Studied by In Situ X-Ray Absorption Spectroscopy. *J. Phys. Chem. B* **2009**, *113*, 10721−10727.
(31) Al Samarai, M.; Hahn, A. W.; Beheshti Askari, A.; Cui, Y. T.; Yamazoe, K.; Miyawaki, J.; Harada, Y.; Rüdiger, O.; Debeer, S. Elucidation of Structure-Activity Correlations in a Nickel Manganese Oxide Oxygen Evolution Reaction Catalyst by Operando Ni L-Edge X-Ray Absorption Spectroscopy and 2p3d Resonant Inelastic X-Ray Scattering. *ACS Appl. Mater. Interfaces* **2019**, *11*, 38595−38605.
(32) Wiese, K.; Abdel-Mageed, A. M.; Klyushin, A.; Behm, R. J. Dynamic Changes of Au/ZnO Catalysts during Methanol Synthesis: A Model Study by Temporal Analysis of Products (TAP) and Zn LIII near Edge X-Ray Absorption Spectroscopy. *Catal. Today* **2019**, *336*, 193−202.
(33) Doh, W. H.; Jeong, W.; Lee, H.; Park, J.; Park, J. Y. Work Function Engineering of SnO Single Crystal Microplates with Thermal Annealing. *Nanotechnology* **2016**, *27*, 335603.
(34) Kurganskii, S. I.; Manyakin, M. D.; Dubrovskii, O. I.; Chuvenkova, O. A.; Turishchev, S. Y.; Domashevskaya, E. P. Theoretical and Experimental Study of the Electronic Structure of Tin Dioxide. *Phys. Solid State* **2014**, *56*, 1748−1753.
(35) Zhang, S.; Yin, C.; Yang, L.; Zhang, Z.; Han, Z. Investigation of the H2 Sensing Properties of Multilayer Mesoporous Pure and Pd-Doped SnO2 Thin Film. *Sens. Actuators, B* **2019**, *283*, 399−406.
(36) Castán-Guerrero, C.; Krizmancic, D.; Bonanni, V.; Edla, R.; Deluisa, A.; Salvador, F.; Rossi, G.; Panaccione, G.; Torelli, P. A Reaction Cell for Ambient Pressure Soft X-Ray Absorption Spectroscopy. *Rev. Sci. Instrum.* **2018**, *89*, 054101.
(37) Kresse, G.; Furthmüller, J. Efficient Iterative Schemes for Ab Initio Total-Energy Calculations Using a Plane-Wave Basis Set. *Phys. Rev. B: Condens. Matter Mater. Phys.* **1996**, *54*, 11169−11186.
(38) Kresse, G.; Furthmüller, J. Efficiency of Ab-Initio Total Energy Calculations for Metals and Semiconductors Using a Plane-Wave Basis Set. *Comput. Mater. Sci.* **1996**, *6*, 15−50.
(39) Kresse, G.; Hafner, J. Ab Initio Molecular Dynamics for Liquid Metals. *Phys. Rev. B* **1993**, *47*, 558−561.
(40) Kresse, G.; Hafner, J. Ab initio molecular-dynamics simulation of the liquid-metal−amorphous-semiconductor transition in germanium. *Phys. Rev. B* **1994**, *49*, 14251−14269.
(41) Perdew, J. P.; Burke, K.; Ernzerhof, M. Generalized Gradient Approximation Made Simple. *Phys. Rev. Lett.* **1996**, *77*, 3865−3868.
(42) Steinmann, S. N.; Corminboeuf, C. A Generalized-Gradient Approximation Exchange Hole Model for Dispersion Coefficients. *J. Chem. Phys.* **2011**, *134*, 044117.
(43) Steinmann, S. N.; Corminboeuf, C. Comprehensive Benchmarking of a Density-Dependent Dispersion Correction. *J. Chem. Theory Comput.* **2011**, *7*, 3567−3577.

https://dx.doi.org/10.1021/acs.jpcc.0c02546
J. Phys. Chem. C 2020, 124, 14202−14212

(44) Perdew, J. P.; Burke, K.; Ernzerhof, M. Generalized Gradient Approximation Made Simple [Phys. Rev. Lett. 77, 3865 (1996)]. *Phys. Rev. Lett.* **1997**, *78*, 1396−1396.
(45) Blöchl, P. E. Projector Augmented-Wave Method. *Phys. Rev. B* **1994**, *50*, 17953−17979.
(46) Reuter, K.; Scheffler, M. Composition, Structure, and Stability of RuO2(110) as a Function of Oxygen Pressure. *Phys. Rev. B: Condens. Matter Mater. Phys.* **2001**, *65*, 035406.
(47) Kravets, V. G. Photoluminescence and Raman Spectra of SnOx Nanostructures Doped with Sm Ions. *Opt. Spectrosc.* **2007**, *103*, 766−771.
(48) Bonu, V.; Das, A.; Amirthapandian, S.; Dhara, S.; Tyagi, A. K. Photoluminescence of Oxygen Vacancies and Hydroxyl Group Surface Functionalized SnO_2 Nanoparticles. *Phys. Chem. Chem. Phys.* **2015**, *17*, 9794−9801.
(49) Mamontov, E.; Vlcek, L.; Wesolowski, D. J.; Cummings, P. T.; Wang, W.; Anovitz, L. M.; Rosenqvist, J.; Brown, C. M.; Garcia Sakai, V. Dynamics and Structure of Hydration Water on Rutile and Cassiterite Nanopowders Studied by Quasielastic Neutron Scattering and Molecular Dynamics Simulations. *J. Phys. Chem. C* **2007**, *111*, 4328−4341.
(50) Mueller, R.; Kammler, H. K.; Wegner, K.; Pratsinis, S. E. OH Surface Density of SiO_2 and TiO_2 by Thermogravimetric Analysis. *Langmuir* **2003**, *19*, 160−165.
(51) Panaccione, G.; Vobornik, I.; Fujii, J.; Krizmancic, D.; Annese, E.; Giovanelli, L.; MacCherozzi, F.; Salvador, F.; De Luisa, A.; Benedetti, D.; et al. Advanced Photoelectric Effect Experiment Beamline at Elettra: A Surface Science Laboratory Coupled with Synchrotron Radiation. *Rev. Sci. Instrum.* **2009**, *80*, 043105.
(52) Thakur, H.; Kumar, R.; Thakur, P.; Brookes, N. B.; Sharma, K. K.; Singh, A. P.; Kumar, Y.; Gautam, S.; Chae, K. H. Orbital Anisotropy in SnO_2 Thin Films and Its Modification by Swift Heavy Ion Irradiation. *Chem. Phys. Lett.* **2011**, *511*, 322−325.
(53) Kucheyev, S. O.; Baumann, T. F.; Sterne, P. A.; Wang, Y. M.; Van Buuren, T.; Hamza, A. V.; Terminello, L. J.; Willey, T. M. Surface Electronic States in Three-Dimensional SnO_2 Nanostructures. *Phys. Rev. B: Condens. Matter Mater. Phys.* **2005**, *72*, 035404.
(54) Ruosi, A.; Raisch, C.; Verna, A.; Werner, R.; Davidson, B. A.; Fujii, J.; Kleiner, R.; Koelle, D. Electron Sampling Depth and Saturation Effects in Perovskite Films Investigated by Soft X-Ray Absorption Spectroscopy. *Phys. Rev. B: Condens. Matter Mater. Phys.* **2014**, *90*, 125120.
(55) Barrus, D. M.; Blake, R. L.; Burek, A. J.; Chambers, K. C.; Pregenzer, A. L. K-Shell Photoabsorption Coefficients of O_2, CO_2, CO and N_2O. *Phys. Rev. A: At., Mol., Opt. Phys.* **1979**, *20*, 1045.
(56) Cabral Tenorio, B. N. C.; Moitra, T.; Nascimento, M. A. C.; Rocha, A. B.; Coriani, S. Molecular Inner-Shell Photoabsorption/Photoionization Cross Sections at Core-Valence-Separated Coupled Cluster Level: Theory and Examples. *J. Chem. Phys.* **2019**, *150*, 224104.
(57) McLaren, R.; Clark, S. A. C.; Ishii, I.; Hitchcock, A. P. Absolute Oscillator Strengths from K-Shell Electron-Energy-Loss Spectra of the Fluoroethenes and 1,3-Perfluorobutadiene. *Phys. Rev. A: At., Mol., Opt. Phys.* **1987**, *36*, 1683−1701.
(58) Latimer, A. A.; Kulkarni, A. R.; Aljama, H.; Montoya, J. H.; Yoo, J. S.; Tsai, C.; Abild-Pedersen, F.; Studt, F.; Nørskov, J. K. Understanding Trends in C-H Bond Activation in Heterogeneous Catalysis. *Nat. Mater.* **2017**, *16*, 225−229.
(59) Elger, A.-K.; Hess, C. Elucidating the Mechanism of Working SnO_2 Gas Sensors Using Combined Operando UV/Vis, Raman, and IR Spectroscopy. *Angew. Chem., Int. Ed.* **2019**, *58*, 15057−15061.

https://dx.doi.org/10.1021/acs.jpcc.0c02546
J. Phys. Chem. C 2020, 124, 14202−14212